nature physics
SUPPLEMENTARY INFORMATION
DOI: 10.1038/NPHYS1438

Materials and Methods

Targets consisted of a ~500 µm-thick diamond disk glued to a 50 µm-thick diamond-turned aluminum disk as shown in figure 1A. A plastic ablator was used to minimize hard x-ray generation in the laser-plasma region. Both single-crystal, natural, type-1a diamond, and poly-crystalline, synthetic, type 2a diamond disks with an average grain size of about 130 µm were used. The polycrystalline diamond wafers were made by chemical vapor deposition (CVD) on a silicon substrate with an initial seed-grain size of ~10 nm; there was little preferred orientation. The density of the diamond was determined to be 3.51 g/cm^3 and the refractive index at 532 nm was $n = 2.42$. The diamond samples were anti-reflection coated (for the 532 nm probe beam) with 81.8 nm of Al_2O_3 on the rear surface.

The OMEGA laser at the University of Rochester[2] was used to produce strong shocks by focusing 1-ns pulses with up to 3 kJ of 351-nm laser light to a flat spot ~600 µm in diameter. A two-channel VISAR diagnostic[5-7] operating at 532 nm measured the shock velocity, *Us*, in the diamond samples. A typical VISAR trace is shown in figure 1B. Fringe positions in the VISAR record are determined to better than 5% of a fringe. *Us*, which ranged from 20 to 42 µm/ns, was measured with <1% accuracy, by choosing appropriate etalons (velocity per fringe of 2.85 and 6.65 km/s). An example velocity history from both velocity interferometers is shown in figure 1B.

The reflectivity of diamond was measured by comparing the intensity of the VISAR signal from the diamond shock to the pre-shock signal from the known aluminum reference. The results from 10 shots are shown in figure 2, inset (a). The reflectivity determined by Bradley et al.[8] is shown in red for comparison. For shock velocities

DOI: 10.1038/NPHYS1438

between 20.5 and 24.5 μm/ns (600 and 1050 GPa) the reflectance of shock-compressed diamond increases rapidly then saturates at R~30%. The optical depth was estimated using a simple metallic Drüde model to be ~0.4 μm at 600 GPa decreasing to ~100 Å at saturation. Atoms undergo >15 oscillations and the pressure decay is very small during the time of shock transit through an optical depth. Thus, the shock is expected to follow the principal Hugoniot and to be in local thermal equilibrium (LTE).

Temperature Measurement:

Using the VISAR collection optics, thermal radiation from the shock front was collected by a streaked optical pyrometer (SOP).[9] The point-spread function (PSR) of the SOP streak camera was measured and is comparable to the emission rise time.[9] In order to get quantitative radiance measurements, the PSR was de-convolved from the signal. The absolute spectral radiance, $I(\lambda)$, of the shock front was measured at two wavelengths, λ= 650 and 450 nm. To determine temperature from the spectral radiance, the throughput of the optical path together with the sensitivity of the streaked optical detector at both wavelengths were absolutely calibrated with a NIST-traceable tungsten-filament lamp. The temperature was determined using the grey-body Planck spectrum,

$$I(\lambda) = \varepsilon\alpha \frac{2\pi hc^2}{\lambda^5}\left(\exp\frac{hc}{\lambda k_B T} - 1\right)^{-1}.$$

Since the spectral band of the SOP band-pass filters (λ= 650 and 450 nm, each with a 100 nm band pass) are narrow compared with the total frequency range of a Planckian source at the relevant temperatures, the wavelength dependence of the SOP was approximated by a δ-function at the centroids of the transmission spectra. This allows the use of the simple calibration equation, $T = \frac{T_0}{\ln(1 + A\varepsilon\alpha/I)}$, where T_0 and A are calibration

parameters that depend on the SOP setup and filter, as described by Miller et al.[9] The emissivity, ε, was calculated from $\varepsilon = 1 - R$ where R was assumed to be independent of wavelength and equal to the shock-front reflectivity measured at 532 nm by the VISAR. The reflectivity used in the analyses is shown by the solid-black line in figure 2A. The grey-shaded area represents the reflectivity error, which is the dominant contribution to the temperature error at high temperatures. The emissivity is $0.7 \le \varepsilon \le 1$ so that errors in the emissivity are at most a ~30% temperature effect. (Note that the drop in reflectivity below *Us*=24 km/s leads to an *increase* in ε and a *drop* in the inferred temperature. The temperature rise in the coexistence region below Us=24 km/s is thus reduced by the loss of reflectivity and would be even more dramatic if the emissivity were assumed to be constant in the analysis.) The diamond absorption factor, α, was used to correct for imperfect anti-reflection coating at the diamond-vacuum interface, and for transient absorption in the diamond when the drive laser fired. The diamond transmission recovered quickly (<4 ns) but based on the VISAR intensity prior to breakout into the diamond, the temperature was corrected for the brief absorption early in the scans at high laser intensity. This observed absorption in diamond is due to photo-excitation by low-level x-radiation associated with the laser drive. (This radiation could conceivably cause pre-heat in the diamond as well. By looking for a correlation between the temperature and the drive intensity we determined an upper bound on the preheat of less than 1000 K.)

Figure 2 shows the measured temperature versus shock velocity for nine experiments: four single-crystal [110] and five CVD micro-crystalline diamond samples. Temperature uncertainties were determined by the estimate of the systematic uncertainties in the pyrometer calibration,[9] the variation in shock reflectivity as shown in the inset to figure 2, and the shot-to-shot temperature reproducibility. Figure 2 shows the weighted mean, $\hat{T} = \sum w_i T_i / \sum w_i$, of the temperature measurements, where the weights

DOI: 10.1038/NPHYS1438

are taken as the reciprocal of the variances, $w_i = 1/\sigma_i^2$. Since shot-to-shot variations dominate the random uncertainties estimated for each shock, the weighted standard deviations, $\hat{\sigma}_{\hat{T}}^2 = \left[\sum w_i \sum w_i \left(T_i - \hat{T}\right)^2\right] \Big/ \left[\left(\sum w_i\right)^2 - \sum w_i^2\right]$ are reported as the uncertainties associated with averaged temperatures.

The experimental setup and analysis of the SOP has a large variation, so the shot-to-shot temperature uncertainties are larger than the relative uncertainties within a shot. To demonstrate the reproducibility of the mixed-phase temperature kink we have applied a small correction to the spectral radiance of each temperature history to overlap the transition temperatures (the correction is completely insignificant above 15,000 K). In figure 2 we report the weighted standard deviation of these corrected temperature histories. The shot-to-shot uncertainties are somewhat larger in the mixed-phase region (~800 K) and better represent our absolute determination of the melt temperature. Thus, while we report the corrected uncertainties in the figures to emphasize the shape of the melt curve, it is the shot-to-shot uncertainties that we report throughout the text of our letter.

Possibility of Superheating:

If the melt transition is fast and the shock front is in equilibrium, then the measured P, T path follows the melt curve within the mixed-phase region. Alternatively, it is possible that melting occurs suddenly from a superheated solid to a pure fluid with no mixed-phase region.[10,11] In the case of diamond, two factors suggest that the melt line is followed through a mixed-phase region and superheating is not a factor. First, there is no rapid change in temperature over a small pressure range as is observed for superheating. It should be noted that the same technique used here previously documented a rapid temperature change consistent with superheating for both quartz and fused silica.[12]

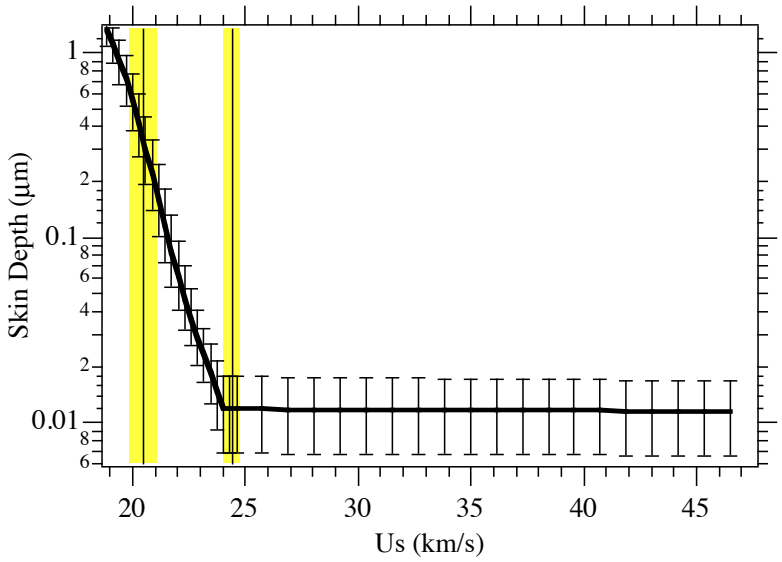

Supporting Figure 1. Skin depth using metallic Drude fit to Reflectivity.

Second, the reflectivity increases smoothly between 600 and 1050 GPa. It was found previously that simple modelling of this reflectivity increase required a conducting-fluid phase with a continuously increasing volume fraction.[8] These observations support the hypothesis of melting along a coexistence curve rather than a superheated solid followed by discontinuous melting (which would imply sudden jumps in both T and $R_{\lambda=532}$).

Simple Metallic Drüde Model:

Previous attempts to model the diamond reflectivity using a thermally-excited semiconductor model could not accurately fit the reflectivity saturation behavior.[8] The model used here is a simpler fit to the reflectivity assuming all reflectivity arises from a metallic fluid phase with a minimum scattering time (Ioffe-Regel limit).[13] The solid phase is insulating and does not contribute to the reflectivity. Reflectivity is calculated using the Fresnel equations, $R = \left|\left(\sqrt{\varepsilon} - n_d\right)/\left(\sqrt{\varepsilon} + n_d\right)\right|^2$ where n_d is the refractive index of un-shocked diamond. The complex dielectric constant of the shocked material,

DOI: 10.1038/NPHYS1438

ε, is calculated from a Drüde formulation such that $\varepsilon = \varepsilon_b - \frac{\omega_p^2}{\omega^2\left(1 + i/\omega\tau\right)}$, where $\varepsilon_b = n_d^2$ represents the bound electron contribution and is assumed to be constant, $\omega_p^2 = \frac{n_e e^2}{\varepsilon_0 m_e}$ is the plasma frequency, and τ is the electron scattering time, which for this analysis is assumed to be equal to the Ioffe-Regel minimum scattering time, $\tau = \tau_{\min} = \frac{2}{v_F}\left(\frac{3}{4\pi n_{atom}}\right)^{1/3}$, where n_{atom} is the atomic density, and v_F is the Fermi velocity. We fit the reflectivity shown in the inset of figure 2 to this model using a single fitting parameter, the electron number density n_e. From this we can calculate the skin depth as the reciprocal of the absorption coefficient, shown in supporting figure 1. This is an estimate of the depth of the region probed in our temperature estimates. We see that the probe is always within 0.01 to 0.4 μm of the shock front. In our letter we note that since the thermal emission originates within a thin skin depth of the shock front, shock melting of pristine diamond was the only transition observed; the material behind the shock was not probed.

Specific Heat Analysis:

The specific heat at constant volume can be determined from measurements of the Hugoniot and the temperature on the Hugoniot. Following previous work[12,14-16] an increment along the Hugoniot can be considered to be the sum of an isentropic compression step and an isochoric heating step such that, $\Delta E_H = \Delta E_S + \Delta E_V$ and $\Delta T_H = \Delta T_S + \Delta T_V$, where the subscript H identifies a change along the Hugoniot, S along an isentrope, and V along an isochore. Then the specific heat is given by,

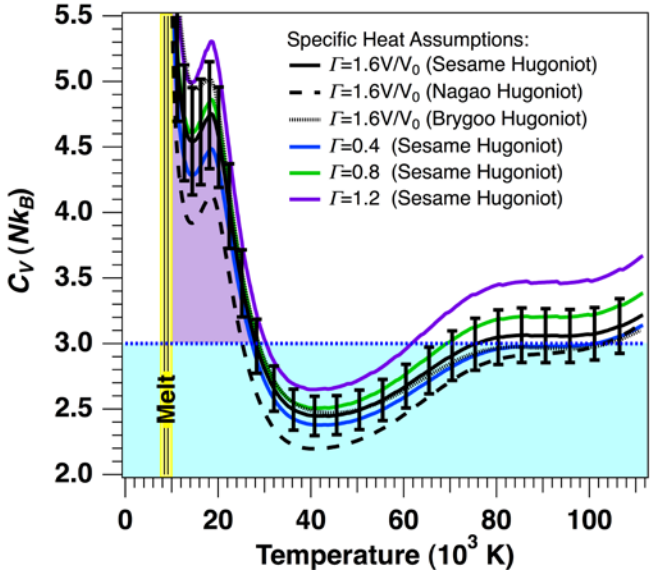

Supporting figure 2. Results for C_V using various behaviours for the properties of conducting fluid carbon. The Hugoniots considered are for the Sesame EOS[1], and the experimental Hugoniots of Nagao et al.[3] and Brygoo et al.[4]

$$C_V = \frac{\Delta E_V}{\Delta T_V} = \frac{\Delta E_H - \Delta E_S}{\Delta T_H - \Delta T_S} = \frac{\left.\frac{\partial E}{\partial V}\right|_H + P}{\left.\frac{\partial T}{\partial V}\right|_H + \Gamma \frac{T}{V}}$$

where the thermodynamic definitions of pressure, $P = -\left.\frac{\partial E}{\partial V}\right|_S$, and the Gruneissen parameter, $\Gamma = -\frac{V}{T}\left.\frac{\partial T}{\partial V}\right|_S$, were used in the derivation. The Hugoniot relation between E, V, and P were obtained from the Sesame equation of state.[1] The temperature is measured here, so that the only parameter that is not directly measured is Γ. However, C_V is quite insensitive to the value of Γ since $\left.\partial T/\partial V\right|_H$ exceeds T/V by a factor of 3 to 6. In other words, the temperature rise along the Hugoniot is large compared to the isentropic temperature rise for strong shocks. We set $\Gamma = 1.6\frac{V}{V_0}$ so that Γ ranges from 0.85 to 0.57 as suggested by recent simulations[17] over range of our experiments.

DOI: 10.1038/NPHYS1438

It is crucial to examine the uncertainties inherent in our estimate of C_V very carefully. The error bars plotted in figure 4 of our letter represent both experimental errors in determining the experimental derivatives as well as systematic uncertainties contributed by assumptions of the Hugoniot and of Γ. We have done so by considering Hugoniots fitted independently to each of the recent experimental measurements of the Hugoniot[3,4], and by setting $\Gamma = 0.4,\ 0.8$, and 1.2. The effect of these reasonable uncertainties in the properties of the conducting fluid are shown in supporting figure 2.

High values of specific heat are similarly observed just above the melt temperatures of quartz, fused-silica,[12] many alkali-halides (including, CsI, CsBr, KBr, KCl, and NaCl),[14] silicon, and germanium,[18-20] and have been interpreted in terms of dissociation of a short-range ordered fluid. The high specific heat of molten Si and Ge[18-20] is correlated with an anomalous (likely tetrahedral) liquid structure factor,[21-29] and there is an explicit relationship between the structure factor and specific heat for a liquid described by pairwise interactions.[30] Thus, the observed peak in C_V is likely due to a reconfiguration of atomic packing, from a partially-bonded complex fluid to an atomic fluid above 60,000 K.

References:

1. Lyon, S.P. and Johnson, J.D., Diamond Sesame Table. *Los Alamos National Laboratory Report No. LA-UR-92-3407* (1992).
2. Boehly, T.R. et al., Initial performance results of the OMEGA laser system. *Opt. Comm.* **133,** 495-506 (1997).
3. Nagao, H. et al., Hugoniot measurement of diamond under laser shock compression up to 2 TPa *Phys. Plasmas* **13,** 052705 (2006).
4. Brygoo, S. et al., Laser-shock compression of diamond and evidence of a negative slope melting curve. *Nature Materials* **6,** 274-277 (2007).
5. Celliers, P.M. et al., Line-imaging velocimeter for shock diagnostics at the OMEGA laser facility *Rev. Sci. Instrum* **75,** 4916-4929 (2004).
6. Barker, L.M. and Hollenbach, R.E., *J. Appl. Phys.* **43,** 4669-4675 (1972).
7. Barker, L.M. and Schuler, K.W., *J. Appl. Phys.* **45,** 3692-3693 (1974).

8. Bradley, D.K. et al., Shock Compressing Diamond to a Conducting Fluid. *Phys. Rev. Lett.* **93,** 195506 (2004).
9. Miller, J.E. et al., Streaked optical pyrometer system for laser-driven shock-wave experiemnts on OMEGA. *Rev. Sci. Instrum* **78,** 034903 (2006).
10. Luo, S.-N. and Ahrens, T.J., Shock-induced superheating and melting curves of geophysically important minerals. *Physics of Earth and Planetary Interiors* **143–144,** 369-386 (2004).
11. Boness, D.A. and Brown, J.M., Bulk superheating of solid KBr and CsBr with shock waves. *Phys. Rev. Lett.* **71,** 2931-2934 (1993).
12. Hicks, D.G. et al., Dissociation of Liquid Silica at High Pressures and Temperatures. *Phys. Rev. Lett.* **97,** 025502 (2006).
13. Goettel, K.A., Eggert, J.H., Silvera, I.F. and Moss, W.C., Optical evidence for the metallization of xenon at 132(5) GPa. *Phys. Rev. Lett.* **62,** 665-668 (1989).
14. Boness, D.A. and Brown, J.M., Heat Capacity of Shocked Alkali Halides, in *Shock Compression of Condensed Matter*, edited by S. C. Schmidt and W. C. Tao (AIP, 1996), Vol. 370, pp. 85-88.
15. Radousky, H.B., Ross, M., Mitchell, A.C. and Nellis, W.J., Shock temperatures and melting in CsI. *Phys. Rev. B* **31,** 1457-1463 (1985).
16. Keeler, R.N. and Royce, E.B., Shock Waves in Condensed Media, in *Physics of High Energy, Density*, edited by P. Caldirola and H. Knoepfel (Academic, New York, 1971), pp. 88.
17. Correa, A.A., Bonev, S.A. and Galli, G., Carbon under extreme conditions: Phase boundaries and electronic properties from first-principles theory *Proc. Nat. Acad. Sci.* **103,** 1204-1208 (2006).
18. Zhou, Z., Mukherjee, S. and Rhim, W.-K., Measurement of thermophysical properties of molten silicon using an upgraded electrostatic levitator. *J. Cryst. Growth* **257,** 350-358 (2003).
19. Rhim, W.-K. and Ohsaka, K., Thermophysical properties measurement of molten silicon by high-temprature electrostatic levitator: density, volume expansion, specific heat capacity, emissivity, surface tension and viscosity. *J. Cryst. Growth* **208,** 313-321 (2000).
20. Rhim, W.-K. and Ishikawa, T., Thermophysical Properties of Molten Germanium Measured by a High-Temperature Electrostatic Levitator. *Internat. J. Thermophys.* **21,** 429-443 (2000).
21. Kahl, G. and Hafner, J., The structure of molten germanium. *Sol. Ste. Commun.* **49,** 1125-1128 (1884).
22. Higuchi, K. et al., Precise measurement of density and structure of undercooled molten silicon by using synchrotron radiation combined with electromagnetic levitation technique. *Meas. Sci. Technol.* **16,** 381-385 (2005).
23. Jakse, N. et al., Structural changes on supercooling liquid silicon. *Appl. Phys. Lett.* **83,** 4734-4736 (2003).

DOI: 10.1038/NPHYS1438

24. Waseda, Y. and Suzuki, K., Structure of molten silicon and germanium by x-ray diffraction. *Z. Phys. B* **20,** 339-343 (1975).
25. Waseda, Y. et al., High Temperature X-Ray Diffraction Study of Melt Structure of Silicon. *Jpn. J. Appl. Phys.* **34,** 4124-4128 (1995).
26. Kimura, H., Watanabe, M., Izumi, K. and Hibiya, T., X-ray diffraction study of undercooled molten silicon. *Appl. Phys. Lett.* **78,** 604-606 (2001).
27. Petkov, V., Takeda, S., Waseda, Y. and Sugiyama, K., Structural study of molten germanium by energy-dispersive X-ray diffraction. *J. Non-Cryst. Sol.* **168,** 97-105 (1994).
28. Hallal, S., Gasser, J.-G. and Grosdidier, B., The structure of molten germanium from *ab initio* pseudopotential-based pair potentials. *J. Non-Cryst. Sol.* **353,** 3495 (2007).
29. Waseda, Y., *The Structure of Non-Crystalline Materials*. (McGraw-Hill, New York, 1980)
30. Goodstein, D.L., *States of Matter*. (Dover, New York, 1985), Eq. 4.3.24.